Chinese Journal of Catalysis 61 (2024) 154–163

available at www.sciencedirect.com

ScienceDirect

journal homepage: www.sciencedirect.com/journal/chinese-journal-of-catalysis

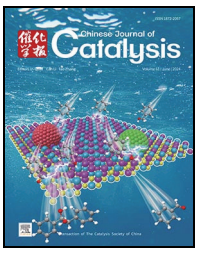

Article

Understanding the correlation between zinc speciation and coupling conversion of CO_2 and *n*-butane on zinc/ZSM-5 catalysts

Xuke Sun [a,b], Rongsheng Liu [a], Gaili Fan [a,c], Yuhan Liu [a,d], Fangxiu Ye [a,b], Zhengxi Yu [a,*], Zhongmin Liu [a,b,*]

[a] *National Engineering Research Center of Lower-Carbon Catalysis Technology, Dalian National Laboratory for Clean Energy, Dalian Institute of Chemical Physics, Chinese Academy of Sciences, Dalian 116023, Liaoning, China*

[b] *University of Chinese Academy of Sciences, Beijing 100049, China*

[c] *School of Chemistry, Dalian University of Technology, Dalian 116024, Liaoning, China*

[d] *College of Chemistry and Chemical Engineering, China University of Petroleum (East China), Qingdao 266580, Shandong, China*

ARTICLE INFO

Article history:
Received 5 March 2024
Accepted 10 April 2024
Available online 20 June 2024

Keywords:
Coupling reaction
CO_2 utilization
Zn-introduced
$Zn\text{-}OH^+$
$(Zn\text{-}O\text{-}Zn)^{2+}$
ZSM-5

ABSTRACT

The coupling reaction of alkanes and CO_2 into high value-added bulk chemical products is a promising way for CO_2 utilization. The Zn-introduced ZSM-5 catalyst plays an essential role in this process; however, the correlation between the catalytic performance and Zn species of the catalyst has yet to be established. Herein, the structural properties, the acid sites, and the existence status of the Zn species in the Zn-introduced catalysts were systematically characterized by several techniques. And the influence of the state of Zn species in the coupling reaction was discussed. The results indicate that the Zn species exist in the form of ZnO cluster, $Zn\text{-}OH^+$, and $(Zn\text{-}O\text{-}Zn)^{2+}$ species, thereinto $(Zn\text{-}O\text{-}Zn)^{2+}$ species are produced by the $Zn\text{-}OH^+$ group with the increasing Zn loading. The decrease of Brønsted acid sites, the formation of newly active sites caused by Zn species, and the accumulation of coarse ZnO species, are responsible for the change of *n*-butane conversion. The $Zn\text{-}OH^+$ group serves as the primary catalytic center for the conversion of CO_2. Both the $Zn\text{-}OH^+$ group and the $(Zn\text{-}O\text{-}Zn)^{2+}$ species enhance the dehydrogenation performance of the Zn-introduced catalysts, thereby promoting the generation of aromatics. The Zn5%-ZSM-5 sample showed the most excellent catalytic performance; the *n*-butane conversion was 94.71%, the CO_2 conversion was 30.43%, and the aromatics selectivity was 53.71%. Simultaneously, we propose a more specific mechanism for the coupling reaction.

1. Introduction

Carbon dioxide (CO_2) utilization has gained significant global attention in recent years due to its potential for addressing environmental concerns [1,2]. Finding effective ways to capture and utilize CO_2 is essential for combating the detrimental effects of climate change by decreasing greenhouse gas emissions. Linking CO_2 to yield bulk chemicals, converting CO_2 into value-added products, and thereby reducing its impact on the environment is currently the main research direction [3,4].

* Corresponding author. E-mail: zhengxiyu@dicp.ac.cn (Z. Yu), liuzm@dicp.ac.cn (Z. Liu).

This work was supported by the National Natural Science Foundation of China (21991093, 21991092, 21991090), the National Key Research and Development Program of China (2022YFE0116000) and the Strategic Priority Research Program of the Chinese Academy of Sciences (XDA29000000).
https://doi.org/10.1016/S1872-2067(24)60036-7

The coupling reaction between low-carbon alkanes and CO_2 to yield aromatics is currently a promising route in research. Aromatics are essential raw materials for the chemical industry and play a vital role in different industries [5,6]. The utilization of CO_2 can be effectively linked with the production of high-value added bulk chemicals using this route. In this route, CO_2 can not only serve as a weak oxidant to regulate the proportion of carbon and hydrogen elements of the final products, but also consume carbon deposits through the reverse Boudouard reaction to extend the lifetime of the catalysts [7].

The coupling reaction between CO_2 and *n*-butane, as one of the routes mentioned above, has received widespread attention in recent years [8–10]. In our previous works, we showed that H-ZSM-5 could catalyze efficiently the coupling reaction of *n*-butane and CO_2, where CO_2 not only acted as a reagent for the hydrogen equilibrium during the coupling reactions but also partially (about one-quarter) was incorporated into aromatic products, revealing the reaction pathway and mechanism of the coupling reaction on H-ZSM-5 [11]. The latest research indicated that modifying H-ZSM-5 zeolite with metal cations could further improve the coupling reaction performance between *n*-butane and CO_2. Among them, the zinc metal-modified H-ZSM-5 catalyst offered the most effective catalytic performance for CO_2 conversion and selectivity of aromatics [10,12].

Recognizing the nature of Zn species in the zeolites is of key importance for understanding their catalytic performances on the coupling reaction of *n*-butane and CO_2. It has been indicated that different Zn species, such as small ZnO clusters, Zn^{2+} cations, and $(Zn\text{-}O\text{-}Zn)^{2+}$ in zeolites, demonstrate different capabilities for the activation of alkanes [13–15]. The Zn^{2+} cations are more efficient in the aromatization, activation, and dehydrogenation of alkane compared to the small ZnO cluster species. Meanwhile, the olefin oligomerization seems to be driven by these Zn species through a mechanism that is different from the conventional oligomerization on the Brønsted acid sites of zeolites [16]. Hitherto, the influence of the Zn species and its relationship with catalytic performance on coupling reactions is still opaque.

In this work, we systematically discussed the coupling reaction of *n*-butane and CO_2 on the Zn-introduced ZSM-5 catalysts to establish the correlation between Zn species and reaction performance. The status of Zn species, including $Zn\text{-}OH^+$, $Zn\text{-}O\text{-}Zn^{2+}$, and ZnO cluster, were qualitatively and quantitatively characterized by several techniques. The change in *n*-butane conversion was due to a comprehensive factor, including the decrease of BASs, the formation of newly active sites attributed to Zn species, and the accumulation of coarse ZnO species. The $Zn\text{-}OH^+$ group was the main catalytic active species for the conversion of CO_2, and both the $Zn\text{-}OH^+$ group and the $(Zn\text{-}O\text{-}Zn)^{2+}$ species possessed strong aromatization performance. Our previous work had extensively investigated the intermediate species and reaction process of the coupling reaction between *n*-butane and CO_2 [10,11,17,18]. Based on this, we further investigated the intrinsic structure-activity relationship on the Zn-introduced ZSM-5 catalysts and refined the reaction mechanism. The results help to further tailor catalyst design for the coupling reaction of *n*-butane and CO_2 with excellent catalytic performance.

2. Experimental

2.1. Catalyst preparation

H-ZSM-5 zeolites were acquired from Nankai University Catalyst Co., Ltd, which possess a Si/Al ratio of 16. $Zn(NO_3)_2{\cdot}6H_2O$ was supplied by Tianjin Damao Chemical Reagent Factory. *n*-Butane (> 99.9%), CO_2 (CO_2, 85.0%; Ar, 15.0%), and nitrogen (> 99.999%) were provided by Dalian Special Gas Co., Ltd.

Zn*x*%-ZSM-5 catalysts, where *x* represented the weight percentage of Zn, were synthesized through an equivalent-volume impregnation method. H-ZSM-5 zeolites were impregnated in a $Zn(NO_3)_2{\cdot}6H_2O$ solution at room temperature for 5 h. The impregnated samples were then dried at 130 °C for 5 h and subsequently calcined at 650 °C for 4 h. The catalysts which are mentioned above were employed for the coupling reaction of *n*-butane with CO_2.

2.2. Catalyst characterization

The X' Pert PRO X-ray powder diffractometer was utilized for conducting X-ray diffraction (XRD) analysis. The analysis involved using 40 kV working voltage and scanning within the range of 5°–50°. The Si, Al, and supported metal contents of the catalyst were determined through X-ray fluorescence analysis (XRF) using an X-ray fluorescence spectrometer which was Philips Magix-601. To examine the structure and size of the samples, a Hitachi SU8020 scanning electron microscope (SEM) equipped with an energy-dispersive X-ray spectroscopy (EDS) analyzer was employed. Nitrogen physical adsorption measurements were carried out using an ASAP-2020 analyzer from the American Mack Company. Fourier transform infrared (FT-IR) spectra were conducted using a Bruker Tensor 27 spectrometer in a transmission mode. The samples were pretreated at 450 °C for 1 h and cooled to 50 °C. Infrared spectroscopy with pyridine adsorption (Py-IR) was performed on a Bruker XF808-04 spectrometer in transmission mode. The spectrometer had a resolution of 4 cm^{-1} and covered a range of 4000–400 cm^{-1}. The diffuse reflectance ultraviolet-visible spectra (DR UV-vis) were measured on a Varian Cary 5000 UV-vis-NIR spectrophotometer. Utilizing the Thermofisher Escalab 250 Xi+ instrument, the X-ray photoelectron spectroscopy (XPS) experiments were conducted. The X-ray was monochromatic Al K_α radiation ($h\upsilon$ = 1486.6 eV). The ^1H MAS NMR spectra of the catalyst sample were determined utilizing a 500 MHz Bruker Avance III spectrometer. The test probe employed a 3.2 mm wvt double-resonance probe with a ^1H resonance frequency of 500.13 MHz.

2.3. Catalyst testing

A reactor was utilized to load 1 g of catalyst sample, which was then placed in the temperature-controlled zone of the reactor. First, the reactor was heated under a flow nitrogen gas,

and adjusted the reaction temperature to 550 °C. Then, simultaneously *n*-butane (99.9%) and CO_2 (CO_2, 85%; Ar, 15%) were fed into the catalyst bed using mass flow controllers with a molar ratio of CO_2/*n*-butane of 0.25 and total mass space velocity of 5 h^{-1}. The coupling reaction was conducted at 550 °C under atmospheric pressure. All the post-reaction products were directed to online chromatographic analysis. Gas chromatography analysis was performed using an Agilent 7890 B instrument equipped with three detectors, including an HP-PLOT/Q capillary column and an HP-FFAP capillary column connected to FID for analysis of the distribution of hydrocarbon products, and a 5A packed column and a porapak Q connected to TCD for CO_2 conversion and other products analysis.

Using Ar as the internal standard, the conversion rate of CO_2 (X_{CO2}) was calculated by Eq. (1), where CO_{2inlet} and $CO_{2outlet}$ represented CO_2 molar concentration at the inlet and the outlet of the reactor, respectively.

$$X_{CO_2} = \frac{CO_{2_{inlet}} - CO_{2_{outlet}}}{CO_{2_{inlet}}} * 100\% \quad (1)$$

The conversion rate of *n*-butane ($X_{n\text{-butane}}$) was calculated by Eq. (2), where $butane_{inlet}$ and $butane_{outlet}$ represented *n*-butane molar fractions of *n*-butane at the inlet and the outlet of the reactor, respectively.

$$X_{n-butane} = \frac{butane_{inlet} - butane_{outlet}}{butane_{inlet}} * 100\% \quad (2)$$

According to the conservation of carbon atoms, oxygen atoms and hydrogen atoms, the selectivity of various products ($Sel_{C_nH_mO_x}$) at the outlet could be calculated according to Eq. (3), where $C_nH_mO_{xoutlet}$ represented the molar fraction of various products at the outlet and $\Sigma_0^n C_nH_mO_{xoutlet}$ represented the summation of the molar fractions of all the various products (not including reactants) at the outlet, respectively.

$$Sel_{C_nH_mO_x} = \frac{C_nH_mO_{x_{outlet}}}{\sum_0^n C_nH_mO_{x_{outlet}}} * 100\% \quad (3)$$

2.4. *In situ spectroscopic study*

The *in-situ* transmission infrared spectra experiments were conducted using a Bruker Tensor 27 FT-IR spectrometer in transmission mode. The infrared cell was subjected to heating with a flow of 30 mL/min N_2, reaching a temperature of 500 °C for 1 h. A blend of *n*-butane, CO_2, and nitrogen was introduced into the infrared cell at a flow rate of 50 mL/min. By subtracting the spectra of the sample framework from the collected spectra, the IR difference spectra were derived.

The *in-situ* ultraviolet spectroscopy experiments were conducted using a Varian Cary 5000 UV-vis-NIR spectrometer that was equipped with a diffuse reflection attachment. The catalyst was loaded into a diffuse reflecting cell containing a CaF_2 window. Subsequently, the UV cell was heated to 450 °C with a nitrogen flow rate of 30 mL/min for 1 h. A mixture of *n*-butane, CO_2, and nitrogen was introduced into the UV cell at a flow rate of 50 mL/min. By subtracting the spectra of the sample framework from the collected spectra, the UV difference spectra were obtained.

3. Results and discussion

3.1. *Structural characteristics*

The commercial H-ZSM-5 zeolites were used as the parent sample to be modified by equivalent-volume impregnation of the Zn source. Three modified samples with different Zn contents were achieved by various treated conditions to under-

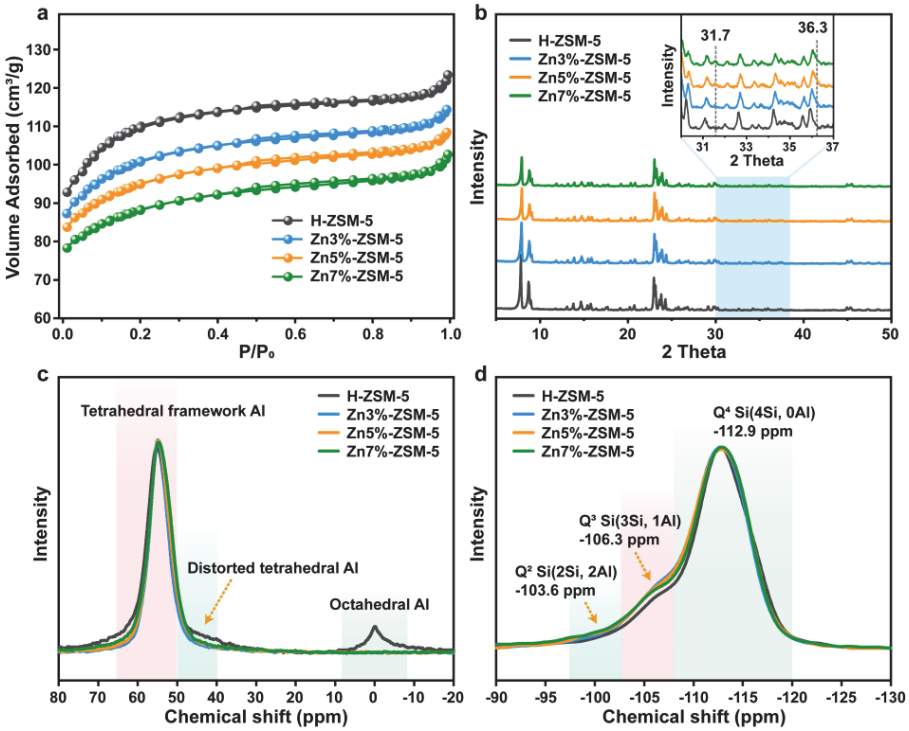

Fig. 1. Characterization results of all samples. (a) N_2 sorption isotherms; (b) XRD patterns; (c) ^{27}Al MAS NMR spectra; (d) ^{29}Si MAS NMR spectra.

stand the correlation between Zn speciation and catalytic performance. Fig. S1 shows the SEM images and corresponding EDS elemental maps of all samples. Samples presented similar regular hexagonal structures with sharp edges and uniform particle sizes (≈1 μm), indicating that the morphology of the samples was not affected by the incorporation of Zn species. And the constituent elements (Si, Al, O, and Zn) exhibited a uniform dispersion (Fig. S1). The XRF and N_2-BET results are given in Fig. 1(a) and Table S1. The XRF results demonstrated that the Zn content of the samples prepared using the equivalent-volume impregnation method was in accordance with the expectation. According to the N_2 adsorption-desorption isotherms, the specific surface area and pore volume were decreased with the increasing Zn loading. This might be owing to some Zn species existing as smaller grains in the channels and on the surface of samples [19]. As shown in Fig. 1(b), the Zn-introduced samples exhibited similar XRD diffraction peaks with H-ZSM-5, indicating that these samples still retained the main MFI topology. However, the primary diffraction peak intensity of the modified samples decreased with the increasing Zn loading, indicating the decreasing relative crystallinity, which was caused by the high X-ray absorption coefficient of Zn species [20–22]. Moreover, it could be seen from the local amplification of the XRD pattern that with the increasing Zn loading (Fig. 1(b)), the diffraction peaks of ZnO species gradually appeared at 2θ = 31.7° and 36.3° in the Zn-introduced samples, inferring the formation of ZnO species [23,24].

^{27}Al and ^{29}Si MAS NMR technology were obtained to trace further the effect of the incorporation of Zn species on the framework of H-ZSM-5 zeolites, and the corresponding spectra of samples were given in Figs. 1(c) and 1(d), respectively. The ^{27}Al MAS NMR spectrum of H-ZSM-5 showed two apparent signals at 55 and 0 ppm, attributed to tetrahedral framework Al and octahedral Al, respectively [25]. Moreover, the signal at 55 ppm emerged a shoulder resonance in the up field (40–50 ppm region), which was connected to the distorted tetrahedral Al [26]. Fig. 1(c) shows that the resonances corresponding to distorted tetrahedral Al and octahedral Al vanished after Zn loading. In the ^{29}Si MAS NMR spectra, the primary signal at −110−−116 ppm was assigned to the Si (4Si, 0Al) species, and the signals at about −106 and −103 ppm could be ascribed to the Si (3Si, 1Al) and Si (2Si, 2Al) species, respectively [27,28]. After the incorporation of Zn in the H-ZSM-5, the intensity of the Si (3Si, 1Al) and Si (2Si, 2Al) resonance signals visibly increased. Based on the results of ^{27}Al and ^{29}Si NMR spectra, we could infer that Zn loading treatment could convert distorted tetrahedral Al and octahedral Al into tetrahedral framework Al, which was reported in many other zeolites [25,29]. However, with the further increasing Zn loading, framework Al was slightly removed, reflected in the ^{29}Si NMR spectra with the decrease of the signal at −106 ppm.

3.2. Zn speciation and acid site characteristics

We focused on the status of Zn species, which were closely relevant to the catalytically active sites of the Zn-introduced H-ZSM-5. Fig. 2(a) shows the DR UV-vis spectra of all samples. For the H-ZSM-5 sample, two adsorption bands at 210 and 268

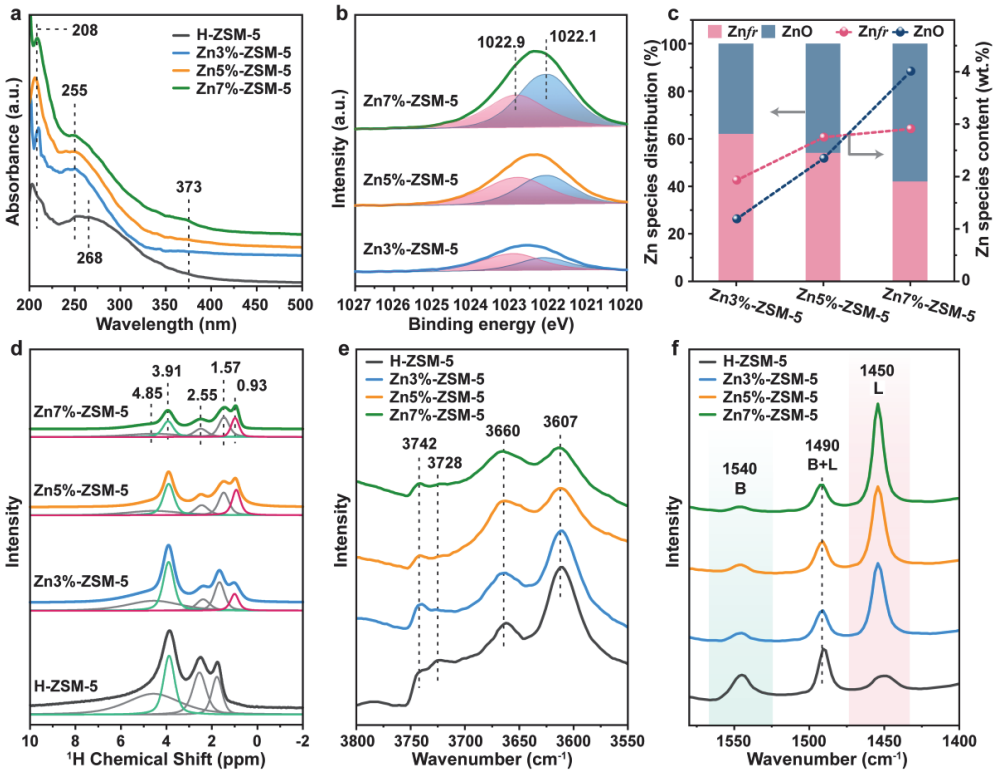

Fig. 2. (a) UV-vis spectra of all samples. (b) XPS spectra of Zn $2p_{3/2}$ for the Zn-introduced samples. (c) The distributions and content of Zn species in the Zn-introduced samples with increasing Zn loading and provided data are determined from the combination of XPS and XRF. (d) ^{1}H MAS NMR spectra with corresponding deconvolution results of all samples. FTIR (e) and Py-FTIR (f) spectra of all samples.

nm were associated with the zeolite structure charge transfer [30,31] and surface defects [32,33], respectively. In the Zn-introduced samples, two absorption bands at 373 and 255 nm were observed, related to ZnO with larger particle size [34] and ZnO cluster with a diameter of about 10 Å [35,36], respectively. With the increasing Zn loading, the band at 373 nm gradually appeared, indicating the formation of large-size ZnO crystal particles, consistent with the XRD results. The band strength at 255 nm firstly increased and then decreased with the increase of Zn loading, which was caused by the transformation of some small ZnO cluster into large ZnO crystal particles. The absorption bands below 230 nm were considered to be the framework Zn species, which strongly interacted with the zeolite framework [37]. In the Zn-introduced ZSM-5 samples, absorption bands below 230 nm were explicitly found, indicating the existence of Zn species that strongly interacted with the framework of zeolites, such as Zn-OH$^+$ and (Zn-O-Zn)$^{2+}$ species. However, the detailed Zn coordination states could not be confirmed by the DR UV-vis spectra.

Furthermore, XPS was utilized to probe the status and structure of Zn species in the Zn-introduced samples (Fig. 2(b)). Different Zn species with two kinds of binding energy were identified by binding energy correction and peak fitting of the XPS spectra. It was plausible to connect the binding energy peak at 1022.1 eV to ZnO species given that the binding energy of pure ZnO species was 1021.8 eV [15,24]. It was possible that the peak of ZnO species shift towards higher binding energy was a result of the interaction between ZnO and the zeolite electronegativity framework [38–40]. Another binding energy peak at 1022.9 eV could be assigned to Zn species that strongly interacted with the protic acid sites on the zeolite framework [24,40,41], including Zn-OH$^+$ and (Zn-O-Zn)$^{2+}$ species. As shown in Fig. 2(c) and Table 1, the relative proportions of ZnO and Zn species on the zeolite framework (Zn_{fr}) were roughly estimated according to their binding energy peak intensity [42]. Meanwhile, combined with the content of Zn in the XRF results, the absolute number of the two main Zn species was calculated. We could conclude that the content of two Zn species increased with the increase of Zn loading, while the proportion of Zn_{fr} decreased continuously. In the Zn7%-ZSM-5 sample, the Zn_{fr}/ZnO was less than 1, indicating that ZnO species dominated. Compared with other Zn-introduced samples, the increasing Zn loading in the Zn7%-ZSM-5 sample was mainly in the form of ZnO species.

The existence forms of Zn species were also explored by ^{1}H MAS NMR spectral analysis (Fig. 2(d)), and deconvolution of the ^{1}H NMR spectra allowed us to quantify the OH species of all samples, the calculated results are given in Table 2. First, we focused on the signal at 0.93 ppm attributed to Zn-OH$^+$ species [43,44]. Remarkably, the concentration of the Zn-OH$^+$ group went up initially, but then decreased with the increase in Zn loading, which reached a maximum in the Zn5%-ZSM-5 sample. The excessive content of Zn metal in the Zn7%-ZSM-5 sample led a partial Zn-OH$^+$ group to form (Zn-O-Zn)$^{2+}$ group, bringing about the decrease of the Zn-OH$^+$ group. Simultaneously, the high content of Zn metal led to the production of many ZnO species, which would also significantly impact the Zn-OH$^+$ group. In conclusion, there were three forms of Zn species present in the Zn-introduced samples: ZnO cluster, (Zn-O-Zn)$^{2+}$, and Zn-OH$^+$, respectively. The content of ZnO and (Zn-O-Zn)$^{2+}$ species increased with the increasing Zn loading, while the content of Zn-OH$^+$ species increased firstly and then decreased, which would be used to establish a correlation with catalytic performances of the Zn-introduced samples.

Table 1
Zn species distribution of the Zn-introduced samples.

Sample	Zn by type			
	Total [a] (wt%)	Zn_{fr} [b] (wt%)	ZnO [b] (wt%)	Zn_{fr}/ZnO [b]
Zn3%-ZSM-5	3.12	1.93	1.19	1.62
Zn5%-ZSM-5	5.10	2.75	2.35	1.17
Zn7%-ZSM-5	6.92	2.91	4.01	0.73

Notes: [a] Zn content of the samples was determined by XRF. [b] Zn species distribution was determined by XPS.

Table 2
OH species concentration of all samples.

Sample	OH concentration/mmol g^{-1}				
	Si-OH-Al$_{(H\text{-}bond)}$	Si-OH-Al	Al-OH	Si-OH	Zn-OH
H-ZSM-5	1.21	0.71	0.62	0.41	0
Zn3%-ZSM-5	0.52	0.52	0.15	0.29	0.17
Zn5%-ZSM-5	0.25	0.36	0.14	0.25	0.19
Zn7%-ZSM-5	0.16	0.14	0.09	0.17	0.07

Another important consideration was the change of acid sites in H-ZSM-5 samples after Zn loading. In Fig. 2(d), the resonance signals at 4.85 and 3.91 ppm were assigned to the Si-OH-Al group with hydrogen bonds and the isolated Si-OH-Al group [45], relevant to the Brønsted acid sites (BASs). The signals at 1.57 and 2.55 ppm were associated with the nonacidic Si-OH group [43] and the extraframework Al-OH [46], respectively. With the increasing Zn loading, the content of Si-OH-Al groups showed a downward trend, suggesting a strong interaction between the incorporated Zn species and BASs in the H-ZSM-5, consistent with the above characterization results. Simultaneously, the amount of the Si-OH and Al-OH groups also decreased after Zn loading.

The significant change in the acid sites of the Zn-introduced samples was also confirmed by the FTIR spectra (Fig. 2(e)). The spectrum of H-ZSM-5 showed a band at 3607 cm^{-1} corresponding to the bridging hydroxyl, representing BASs [23]. It was not difficult to find that the band at 3607 cm^{-1} gradually decreased with the increasing Zn loading, attributed to the bridging hydroxyl group replaced by the introduced Zn species. The Zn species exchanged with protons at this location to form the Zn-OH$^+$ species [47,48]. The extra-framework Al-OH corresponding to the band at 3660 cm^{-1} could be found in zeolites [49], whose intensity showed a change with the increasing Zn content, speculated to be caused by the interaction between ZnO and Al-OH [50]. The bands at 3728 and 3742 cm^{-1} were attributed to the free internal silanol group and the isolated external silanol group of the zeolites, respectively [23,24]. The isolated external silanol group was less affected by Zn species, while the free internal silanol group was significantly reduced due to its interaction with Zn-OH$^+$ at the cation position [51].

The content of acids with different strengths was obtained

Table 3
Acidic properties of all samples.

Sample	Acidity by strength [a] (mmol g^{-1})			Acidity by type [b] (mmol g^{-1})		
	Strong	Weak	Total	Brønsted	Lewis	B/L
H-ZSM-5	0.509	0.763	1.272	0.775	0.497	1.56
Zn3%-ZSM-5	0.404	0.863	1.267	0.140	1.127	0.12
Zn5%-ZSM-5	0.349	0.906	1.255	0.113	1.142	0.10
Zn7%-ZSM-5	0.331	0.917	1.248	0.067	1.181	0.06

[a] The acidity by strength was determined by NH_3-TPD (strong, NH_3 desorbed at 350–700 °C; weak, NH_3 desorbed at 100–350 °C). [b] The acidity by type was determined by Py-FTIR.

by calculating the adsorption capacity of NH_3 at different temperature stages by NH_3-TPD (Fig. S2), and the calculated results are given in Table 3. The desorption peak position at below 350 °C was a result of NH_3 being absorbed from weak acid sites, while NH_3 desorption from strong acid sites was responsible for the peaks above 350 °C. By comparison with the parent H-ZSM-5, the strong acid sites of the Zn-introduced samples decreased significantly due to the interaction between bridge hydroxyl and Zn species in H-ZSM-5. Meanwhile, a new weak acid center appeared at about 280 °C, indicating that the H-ZSM-5 formed new acid sites caused by incorporating Zn species [24]. The FTIR after pyridine adsorption (Py-FTIR) was used to evaluate the change of Brønsted and Lewis acid sites in all samples based on the areas of absorption bands at 1540 and 1450 cm^{-1}, respectively [52,53]. Based on the Py-FTIR spectra of all samples (Fig. 2(f)) and calculated results (Table 3), with the increasing Zn loading, the BASs showed a gradually decreasing trend, while the Lewis acid sites (LASs) remarkably increased. This was due to the formation of new LASs caused by the incorporation of Zn species. Based on the NH_3-TPD profiles, it could be inferred that the newly generated weak acid sites at 280 °C were LASs owing to the Zn species.

3.3. *Catalytic performance of all samples*

The coupling reaction performances of different samples for the *n*-butane and CO_2 coupling reaction systems were investigated. Fig. 3 shows the conversion of CO_2 and *n*-butane and the distribution of main products in the coupling reaction. With the increasing Zn loading, the *n*-butane conversion was slightly

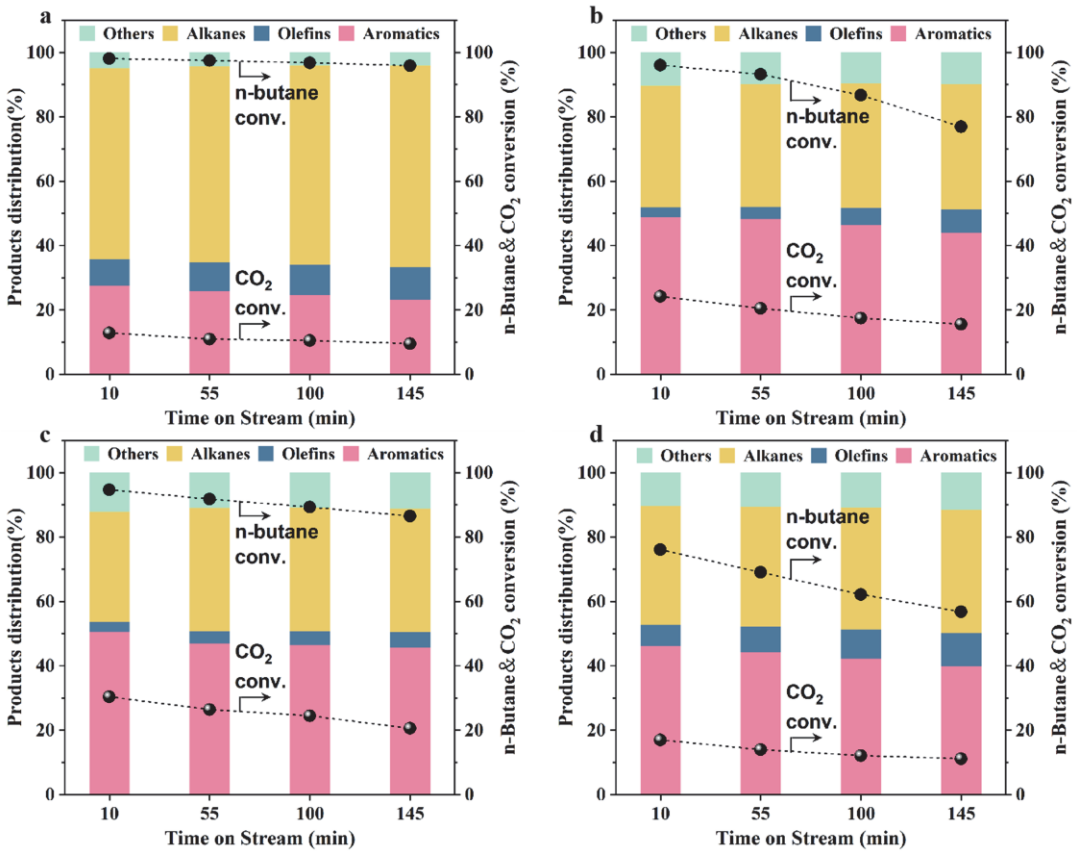

Fig. 3. Catalytic performances of coupling reaction on all samples with the time on stream (TOS). (a) H-ZSM-5; (b) Zn3%-ZSM-5; (c) Zn5%-ZSM-5; (d) Zn7%-ZSM-5. Reaction conditions: 1 g sample, P = 1 bar, T = 550 °C, total WHSV = 5 h^{-1} ($WHSV_{n\text{-butane}}$ = 4.20 h^{-1}, $WHSV_{CO2}$ = 0.80 h^{-1}), CO_2/*n*-butane = 0.25 (molar ratio), TOS = 145 min. Notes: The product distribution of aromatics and others were shown in Figs. S5 and S6, respectively. The detailed product distribution, reactant conversion, and important product selectivity were shown in Tables S2 and S3.

decreased but could remain at a high conversion level, possibly due to a comprehensive factor, including the decrease of BASs and the formation of newly active sites attributed to Zn species. However, the *n*-butane conversion of the Zn7%-ZSM-5 sample decreased significantly. Combined with the above characterization results, it could be inferred that the substantial decrease of the *n*-butane conversion might be due to the accumulation of coarse ZnO species, which would block the channels of zeolites and cover a certain amount of catalytic sites and ultimately lead to the blockage of the *n*-butane diffusion in the Zn7%-ZSM-5 sample.

The conversion of CO_2 had been significantly improved after Zn loading since the Zn species have a strong CO_2 adsorption capacity and could provide a favorable environment for further CO_2 conversion, which was proved by the two CO_2 desorption peaks at around 150 and 450 °C in CO_2-TPD profiles of the Zn-introduced samples (Fig. S3). The conversion of CO_2 first increased and then decreased with the increasing Zn loading, which was highly consistent with the changing trend of the Zn-OH^+ group. Fig. S4 shows the excellent positive correlation between CO_2 conversion and Zn-OH^+ concentration in the coupling reaction, suggesting that the Zn-OH^+ species in the Zn-introduced catalysts could availably promote the conversion of CO_2. Combined with the above characterization results, it could be inferred that the decrease of the CO_2 conversion in the Zn7%-ZSM-5 sample might be due to the formation of $(Zn\text{-}O\text{-}Zn)^{2+}$ species, which led to the decrease of the active Zn-OH^+ group. Therefore, we could infer that the Zn-OH^+ group was the main catalytic active species for the conversion of CO_2.

As shown in Figs. 3 and S4, the selectivity of aromatics also had been significantly improved after Zn loading, and this selectivity climbed up and then declined with the increasing Zn loading, similar to the variation trend of the Zn-OH^+ group, inferring that the Zn-OH^+ group was also beneficial for the generation of aromatics. Interestingly, although the variation trend of the Zn-OH^+ group was consistent with the aromatics selectivity, the corresponding change amplitude was distinct. Compared with the Zn5%-ZSM-5 sample, although the aromatics selectivity also decreased in the Zn7%-ZSM-5 sample, the decrease was relatively little, which was not commensurate with the change of the Zn-OH^+ group. Therefore, we speculated that the Zn-OH^+ group was not the only catalytic active Zn species for the formation of aromatics.

The formation of aromatics is through a complex reaction process, including dehydrogenation, olefins polymerization and cyclization, etc. [54]. As shown in Fig. S7, it was clear that the selectivity of (aromatics + olefins) was almost linear with the H_2 selectivity in all samples, while the H_2 selectivity of the catalysts was closely related to the dehydrogenation, which was inseparably associated with Zn species. Compared with the H-ZSM-5 sample, the main generation path of aromatics on the Zn-introduced samples changed from the hydrogen transfer path to the dehydrogenation path after the Zn species replacing BASs [54]. Therefore, the H_2 selectivity was intimately related to the aromatization performance of the Zn-introduced samples. We attempted to correlate the concentration of the Zn_{fr} [Zn-OH^+ + $(Zn\text{-}O\text{-}Zn)^{2+}$] obtained from ^1H MAS NMR and XPS with the H_2 selectivity, and the results were shown in Fig. S8. The concentration of the Zn_{fr} species in the Zn-introduced samples was almost linearly related to the H_2 selectivity. Based on the above relationships, the structure-performance relationship was established, which confirmed that both the Zn-OH^+ group and the $(Zn\text{-}O\text{-}Zn)^{2+}$ species possessed strong aromatization performance, and the increase of their concentration was conducive to the generation of aromatic products in the coupling reaction.

It is noteworthy that on the H-ZSM-5 sample, the CO produced/CO_2 consumed (molar ratio) was less than 1 as shown in Table S4, indicating that CO_2 could not only be consumed through reverse water-gas shift (RWGS) reaction but also partly incorporated into the aromatic products through complex reactions, which has been demonstrated in our previously published work [11]. Additionally, the CO produced/CO_2 consumed (molar ratio) was more than 1 after Zn loading, which indicated that on the Zn-introduced samples, in addition to the above two reaction paths including RWGS reaction and incorporating into the aromatic products [10], a small part of CO_2 was converted through dry reforming with hydrocarbons to generate more CO.

Fig. 3 also shows the conversion of CO_2 and *n*-butane in all samples as a function of reaction time. With the continuous progress of the reaction, the catalytic performance of the Zn-introduced samples showed an apparent decline, while the H-ZSM-5 sample could maintain relative stability. This phenomenon showed that introducing Zn species made samples have higher reactivity, but the stability was limited. The occurrence of this phenomenon was because the Zn-OH^+ group and $(Zn\text{-}O\text{-}Zn)^{2+}$ species promoted the generation of aromatics in the reaction system, which in turn increased the carbon deposition and ultimately led to the accelerated deactivation of the catalyst. In brief, the Zn-introduced catalysts could effectively promote the conversion of CO_2 and improve the aromatics selectivity of the reaction products.

To investigate the potential regeneration performance of the Zn-introduced ZSM-5 catalysts on the coupling reaction, the regeneration experiments were conducted. A comparison of the catalytic performance among the first, second, and third runs is shown in Fig. S9. It is not difficult to see that after the regeneration test, the catalytic performance of the catalyst can still be maintained at a high level, with high *n*-butane conversion, CO_2 conversion, and aromatics selectivity, indicating that the Zn-introduced samples have good regenerability and reusability.

3.4. Reaction mechanism for the coupling reaction on the Zn-introduced catalysts

Figs. S10 and S11 show the infrared spectrum and ultraviolet spectrum of the coupling reaction on the Zn5%-ZSM-5 sample over time in the different atmospheres, which were used to investigate the reaction mechanism for the coupling reaction of *n*-butane and CO_2. The appearance of absorption peaks at 1850, 1790, 1740, and 1685 cm^{-1} in Fig. S10(b), and the absorption bands at 210–230 and 310–340 nm in Fig. S11 indicated that

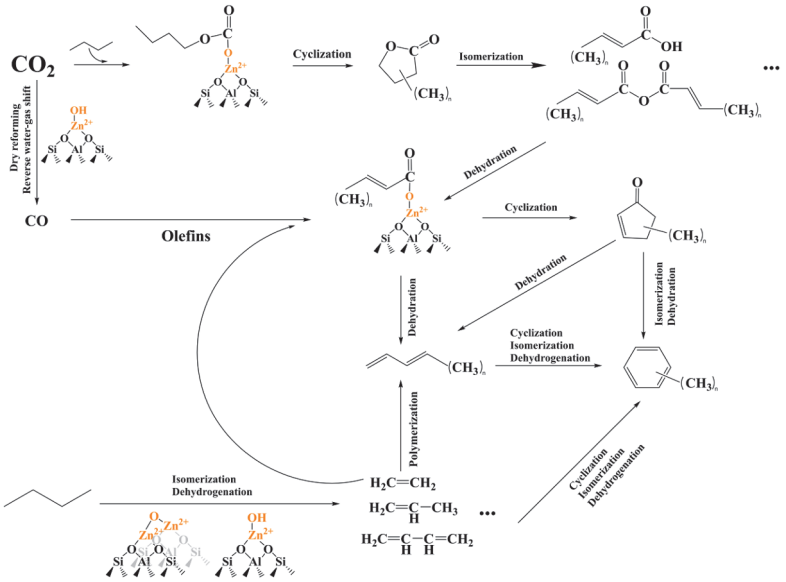

Fig. 4. Proposed mechanism for the coupling reaction on the Zn-introduced catalysts.

during the coupling reaction of *n*-butane and CO_2, anhydrides, lactones, unsaturated aldehydes and ketones and other oxygen-containing intermediate species were generated [18,55–58], and these intermediates played a significant role in the formation of the final target products. Combining the above results of the *in-situ* experiments and the confirmed structure-performance relationship with the research achievements of our previously published work [10,11,17,18], we proposed a more specified reaction mechanism of the coupling reaction as shown in Fig. 4.

CO_2 and *n*-butane could be activated by the Zn-OH^+ species and reacted to form lactones, then lactones formed carboxylic acid, acid anhydride and other oxygen-containing compounds by ring-opening process. These oxygen-containing compounds were then dehydrated by the Zn-OH^+ species to produce unsaturated aldehydes and ketones, which were finally further generated into aromatic hydrocarbon products through a series of intricate reactions [10]. Simultaneously, the Zn-OH^+ group not only had the function of dehydrogenation, but also was the catalytic active species for the RWGS reaction and the dry reforming reaction between CO_2 and hydrocarbons, which produced more CO, and an amount of CO also could enter the aromatic products through a variety of complex reactions [17,18]. Since the $(Zn\text{-}O\text{-}Zn)^{2+}$ species possessed strong aromatization performance but was not the main active species for CO_2 conversion, we speculated that the $(Zn\text{-}O\text{-}Zn)^{2+}$ species mainly catalyze *n*-butane to olefins through dehydrogenation and isomerization, then olefins could produce aromatic products through polymerization, cyclization, dehydrogenation and other processes [10].

4. Conclusions

In summary, the Zn-introduced samples, obtained by equivalent-volume impregnation, provided an excellent catalytic environment for the coupling reaction of *n*-butane and CO_2. When Zn sources were introduced into H-ZSM-5 zeolite, Zn gradually interacted with the BASs to form the Zn-OH^+, $(Zn\text{-}O\text{-}Zn)^{2+}$, and ZnO cluster groups. The BASs were replaced, and the new LASs were formed synchronously. And partial Zn-OH^+ formed the $(Zn\text{-}O\text{-}Zn)^{2+}$ with the increasing Zn loading, bringing about the decrease of Zn-OH^+ group. In consequence, the $(Zn\text{-}O\text{-}Zn)^{2+}$ and ZnO species increased with the increasing Zn loading, while the content of Zn-OH^+ species increased first and then decreased. For the coupling reaction of *n*-butane and CO_2, the conversion of *n*-butane was synergistically influenced by the decrease of BASs, the formation of newly active sites corresponding to Zn species, and the accumulation of coarse ZnO species. The CO_2 conversion and aromatics selectivity climbed up and then declined with the increasing Zn loading. The Zn-OH^+ species was the main active sites for CO_2 conversion through the insertion of CO_2 into aromatics, the reverse water-gas shift reaction, and the dry reforming reaction. Furthermore, the Zn-OH^+ and $(Zn\text{-}O\text{-}Zn)^{2+}$ species possessed strong aromatization performance owing to the excellent dehydrogenation capacity. During the coupling reaction, oxygen compounds such as lactones, unsaturated aldehydes, ketones and anhydrides would be produced as intermediate species. Clarifying the Zn active sites and reaction pathway provide essential guidance for the synthesis and preparation of efficient catalysts for producing value-added chemical reactions using CO_2 and low-carbon alkanes, which may have excellent practical prospects.

Electronic supporting information

Supporting information is available in the online version of this article.

References

[1] M. B. Ansari, S.-E. Park, *Energy Environ. Sci.*, **2012**, 5,

Graphical Abstract

Chin. J. Catal., 2024, 61: 154–163 doi: 10.1016/S1872-2067(24)60036-7

Understanding the correlation between zinc speciation and coupling conversion of CO_2 and *n*-butane on zinc/ZSM-5 catalysts

Xuke Sun, Rongsheng Liu, Gaili Fan, Yuhan Liu, Fangxiu Ye, Zhengxi Yu *, Zhongmin Liu *
Dalian Institute of Chemical Physics, Chinese Academy of Sciences;
University of Chinese Academy of Sciences;
Dalian University of Technology;
China University of Petroleum (East China)

This work established the correlation between Zn species and the catalytic performance of the catalyst, which had a guiding effect on preparing and modifying catalysts for the coupling reaction of CO_2 and alkanes.

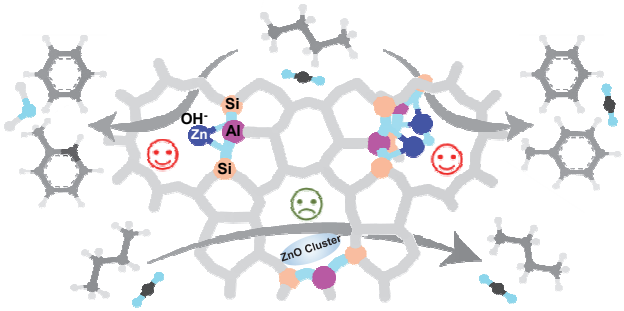

The coupling reaction of n-butane and CO_2 on Zn-ZSM-5

9419–9437.
[2] R. Snoeckx, A. Bogaerts, *Chem. Soc. Rev.*, 2017, 46, 5805–5863.
[3] Z.-Z. Yang, L.-N. He, J. Gao, A.-H. Liu, B. Yu, *Energy Environ. Sci.,* **2012**, 5, 6602–6639.
[4] W. Leitner, *Angew. Chem. Int. Ed.,* **1995**, 34, 2207–2221.
[5] R. A. F. Tomás, J. C. M. Bordado, J. F. P. Gomes, *Chem. Rev.,* **2013**, 113, 7421–7469.
[6] D. Miao, Y. Ding, T. Yu, J. Li, X. Pan, X. Bao, *ACS Catal.,* **2020**, 10, 7389–7397.
[7] E. Gomez, X. Nie, J. H. Lee, Z. Xie, J. G. Chen, *J. Am. Chem. Soc.,* **2019**, 141, 17771–17782.
[8] P. He, J. S. Jarvis, S. Meng, Q. Li, G. M. Bernard, L. Liu, X. Mao, Z. Jiang, H. Zeng, V. K. Michaelis, H. Song, *Appl. Catal. B,* **2019**, 250, 99–111.
[9] J. A. Biscardi, E. Iglesia, *Catal. Today,* **1996**, 31, 207–231.
[10] K. Yang, J. Li, C. Wei, Z. Zhao, Z. Liu, *ACS Catal.,* **2023**, 13, 10405–10417.
[11] C. Wei, W. Zhang, K. Yang, X. Bai, S. Xu, J. Li, Z. Liu, *Chin. J. Catal.,* **2023**, 47, 138–149.
[12] M.Aresta, A. Dibenedetto, E. Quaranta, *J. Catal.*, **2016**, 343, 2–45.
[13] A. A. Gabrienko, S. S. Arzumanov, Z. N. Lashchinskaya, A. V. Toktarev, D. Freude, J. Haase, A. G. Stepanov, *J. Catal.,* **2020**, 391, 69–79.
[14] S. S. Arzumanov, A. A. Gabrienko, A. V. Toktarev, Z. N. Lashchinskaya, D. Freude, J. Haase, A. G. Stepanov, *J. Phys. Chem. C,* **2019**, 123, 30473–30485.
[15] A. A. Gabrienko, S. S. Arzumanov, A. V. Toktarev, I. G. Danilova, I. P. Prosvirin, V. V. Kriventsov, V. I. Zaikovskii, D. Freude, A. G. Stepanov, *ACS Catal.,* **2017**, 7, 1818–1830.
[16] A. A. Gabrienko, S. S. Arzumanov, A. V. Toktarev, D. Freude, J. Haase, A. G. Stepanov, *J. Phys. Chem. C,* **2019**, 123, 27573–27583.
[17] Z. Chen, Y. Ni, Y. Zhi, F. Wen, Z. Zhou, Y. Wei, W. Zhu, Z. Liu, *Angew. Chem. Int. Ed.,* **2018**, 57, 12549–12553.
[18] C. Wei, J. Li, K. Yang, Q. Yu, S. Zeng, Z. Liu, *Chem Catal.,* **2021**, 1, 1273–1290.
[19] X. Niu, J. Gao, K. Wang, Q. Miao, M. Dong, G. Wang, W. Fan, Z. Qin, J. Wang, *Fuel Process. Technol.,* **2017**, 157, 99–107.
[20] Y. Ni, W. Peng, A. Sun, W. Mo, J. Hu, T. Li, G. Li, *J. Ind. Eng. Chem.,* **2010**, 16, 503–505.
[21] H. A. Zaidi, K. K. Pant, *Catal. Today,* **2004**, 96, 155–160.
[22] B. Yu, C. Ding, J. Wang, Y. Zhang, Y. Meng, J. Dong, H. Ge, X. Li, *J. Phys. Chem. C,* **2019**, 123, 18993–19004.
[23] X. Chen, M. Dong, X. Niu, K. Wang, G. Chen, W. Fan, J. Wang, Z. Qin, *Chin. J. Catal.,* **2015**, 36, 880–888.
[24] X. Niu, J. Gao, Q. Miao, M. Dong, G. Wang, W. Fan, Z. Qin, J. Wang, *Microporous Mesoporous Mater.,* **2014**, 197, 252–261.
[25] R. Liu, B. Fan, Y. Zhi, C. Liu, S. Xu, Z. Yu, Z. Liu, *Angew. Chem. Int. Ed.,* **2022**, 61, e202210658.
[26] M. Ravi, V. L. Sushkevich, J. A. van Bokhoven, *Chem. Sci.,* **2021**, 12, 4094–4103.
[27] K. Iyoki, K. Kikumasa, T. Onishi, Y. Yonezawa, A. Chokkalingam, Y. Yanaba, T. Matsumoto, R. Osuga, S. P. Elangovan, J. N. Kondo, A. Endo, T. Okubo, Toru Wakihara, *J. Am. Chem. Soc.,* **2020**, 142, 3931–3938.
[28] R. Liu, S. Zeng, T. Sun, S. Xu, Z. Yu, Y. Wei, Z. Liu, *ACS Catal.,* **2022**, 12, 4491–4500.
[29] M. Ravi, V. L. Sushkevich, J. A. van Bokhoven, *Nat. Mater.*, **2020**, 19, 1047–1056.
[30] A. Sultana, T. Nanba, M. Haneda, M. Sasaki, H. Hamada, *Appl. Catal. B,* **2010**, 101, 61–67.
[31] V. Petranovskii, E. Stoyanov, V. Gurin, N. Katada, M. A. Hernandez, M. Avalos, A. Pestryakov, F. C. Rivas, R. Z. Ulloa, R. Portillo, *Rev. Mex. Fis.,* **2013**, 59, 170–185.
[32] J. T. Kloprogge, *J. Porous Mater.,* **1998**, 5, 5–41.
[33] F. Basile, G. Fornasari, M. Gazzano, A. Vaccari, *Appl. Clay Sci.,* **2000**, 16, 185–200.
[34] S. Bordiga, C. Lamberti, G. Ricchiardi, L. Regli, F. Bonino, A. Damin, K.-P. Lillerud, M. Bjorgen, A. Zecchina, *Chem. Commun.,* **2004**, 2300–2301.
[35] M. Haase, H. Weller, A. Henglein, *J. Phys. Chem.,* **1988**, 92, 482–487.
[36] J. Liu, A. S. N. L. Hong, N. He, G. Liu, C. Liang, X. Zhang, H. Guo, *Chem. Eng. J.,* **2013**, 218, 1–8.
[37] L. Wang, S. Sang, S. Meng, Y. Zhang, Y. Qi, Z. Liu, *Mater. Lett.,* **2007**, 61, 1675–1678.
[38] J. Chen, Z. C. Feng, P. L. Ying, C. Li, *J. Phys. Chem. B,* **2004**, 108, 12669–12676.
[39] E. A. Pidko, R. A. van Santen, *J. Phys. Chem. C,* **2007**, 111, 2643–2655.
[40] Y. Han, J. Yu, T. Chen, X. Liu, L. Sun, *J. Energy Inst.,* **2021**, 94, 210–221.

[41] X. Shang, G. Liu, X. Su, Y. Huang, T. Zhang, *ACS Catal.,* **2022**, 12, 13741–13754.
[42] R. Geng, Y. Liu, Y. Guo, P. Wang, M. Dong, S. Wang, J. Wang, Z. Qin, W. Fan, *ACS Catal.,* **2022**, 12, 14735–14747.
[43] M. Avramovska, D. Freude, J. Haase, A. V. Toktarev, S. S. Arzumanov, A. A. Gabrienko, A. G. Stepanov, *Phys. Chem. Chem. Phys.,* **2023**, 25, 28043–28051.
[44] G. Qi, Q. Wang, J. Xu, J. Trébosc, O. Lafon, C. Wang, J.-P. Amoureux, F. Deng, *Angew. Chem. Int. Ed.*, **2016**, 55, 15826–15830.
[45] A. Stepanov, in: *Zeolites and zeolite-like materials*, B. F. Sels, L. M. Kustov eds., Elsevier, **2016**, 137–188.
[46] M. Hunger, *Catal. Rev. Sci. Eng.*, **1997**, 39, 345–393.
[47] A. Mehdad, R. F. Lobo, *Catal. Sci. Technol.,* **2017**, 7, 3562–3572.
[48] Y. Yuan, R. F. Lobo, *ACS Catal.,* **2023**, 13, 4971–4984.
[49] N. M. Phadke, M. J. Van der, E. Mansoor, A. B. Getsoian, M. Head-Gordon, A. T. Bell, *ACS Catal.,* **2018**, 8, 6106–6126.
[50] Y. G. Kolyagin, V. V. Ordomsky, Y. Z. Khimyak, A. I. Rebrov, F. Fajula, I. I. Ivanova, *J. Catal.,* **2006**, 238, 122–133.
[51] E. M. El-Malki, R. A. van Santen, W. M. H. Sachtler, *J. Phys. Chem. B,* **1999**, 103, 4611–4622.
[52] L. C. Lerici, M. S. Renzini, U. Sedran, L. B. Pierella, *Energy Fuels,* **2013**, 27, 2202–2208.
[53] R. Buzzoni, S. Bordiga, G. Ricchiardi, C. Lamberti, A. Zecchina, G. Bellussi, *Langmuir,* **1996**, 12, 930–940.
[54] D. Liu, L. Cao, G. Zhang, L. Zhao, J. Gao, C. Xu, *Fuel Process. Technol.,* **2021**, 216, 106770.
[55] G. Xiaohong, C. Q. Yang, *Text. Res. J.,* **2000**, 70, 64–70.
[56] T. Forester, R. F. Howe, *J. Am. Chem. Soc.,* **1987**, 109, 5076–5082.
[57] J.-Y. Zhou, G.-D. Lu, S.-H. Wu, *Synth. Commun.*, **1992**, 22, 481–487.
[58] C. Lievens, D. Mourant, M. He, R. Gunawan, X. Li, C.-Z. Li, *Fuel,* **2011**, 90, 3417–3423.

Zn/ZSM-5催化剂中Zn物种与CO_2和正丁烷耦合反应间相关性研究

孙旭科[a,b], 刘荣升[a], 范改丽[a,c], 刘昱含[a,d], 叶芳秀[a,b], 于政锡[a,*], 刘中民[a,b,*]
[a]中国科学院大连化学物理研究所, 洁净能源国家实验室, 低碳催化技术国家工程研究中心, 辽宁大连116023
[b]中国科学院大学, 北京100049
[c]大连理工大学化学学院, 辽宁大连116024
[d]中国石油大学(华东)化学化工学院, 山东青岛266580

摘要: 随着全球温室气体排放的持续增长, 二氧化碳(CO_2)的高效转化与利用已成为应对气候变化、推动可持续发展的重要途径之一. 在本课题组的前期研究中, 以正丁烷为模型化合物, 成功实现了H-ZSM-5分子筛催化CO_2与正丁烷发生耦合反应. 实验还发现, 通过对H-ZSM-5进行Zn改性, 可以显著提高其催化性能, 这为CO_2的高效转化和利用提供了新的研究方向. 然而, 目前关于Zn-ZSM-5催化剂中Zn物种的具体存在状态及其与耦合反应性能之间的关系尚不明确, 这限制了高效催化剂的进一步设计. 因此, 深入探究Zn物种在Zn-ZSM-5催化剂中的存在状态及其与催化性能之间的关联机制, 从而设计和开发更高效的CO_2转化催化剂已成为当务之急.

本文通过紫外-可见光漫反射光谱、X-射线光电子能谱和^{1}H魔角旋转-核磁共振等多种技术系统地表征了Zn-ZSM-5分子筛中酸性中心和Zn物种存在状态的演变过程, 讨论了Zn物种活性中心与耦合反应之间的构-效关系, 阐明了耦合反应的机理. 研究表明, Zn-ZSM-5分子筛中Zn物种主要以ZnO团簇、Zn-OH$^+$和(Zn-O-Zn)$^{2+}$的形式存在, 且其含量随Zn负载量的变化而改变. 其中, ZnO团簇及(Zn-O-Zn)$^{2+}$物种的含量随Zn负载量的增加而上升, 而Zn-OH$^+$物种含量则先上升后下降, 这是由于部分Zn-OH$^+$物种转化为(Zn-O-Zn)$^{2+}$物种. 在CO_2与正丁烷的耦合反应中, 正丁烷的转化受到Brønsted酸位点的减少、Zn活性位点的形成以及粗晶ZnO物种的堆积等多种因素的影响. Zn-OH$^+$物种是主要的CO_2催化转化活性中心, 而芳烃的生成则主要受Zn-OH$^+$和(Zn-O-Zn)$^{2+}$物种的影响. Zn-OH$^+$和(Zn-O-Zn)$^{2+}$物种均具有较强的脱氢性能, 可通过脱氢路径促进芳烃的生成. Zn5%-ZSM-5 (Zn负载量为5 wt%)样品表现出最优的催化性能: 正丁烷转化率为94.71%, CO_2转化率为30.43%, 芳烃选择性为53.71%. 原位实验进一步证实了内酯、羧酸和不饱和醛酮等含氧化合物作为中间体的存在. 基于上述研究, 我们提出了Zn-ZSM-5上CO_2和正丁烷耦合的反应机理, 主要包括以下三条反应路径: (1) 在Zn-OH$^+$物种的催化作用下, 正丁烷和CO_2首先被耦合活化形成内酯, 随后经过一系列反应形成羧酸、酸酐和其他含氧化合物, 最终通过复杂的反应生成芳烃. (2) 部分CO_2在Zn-OH$^+$物种的催化下, 通过逆水煤气变换(RWGS)反应以及与烃类化合物的干重整反应生成CO. 这些CO随后在Zn-OH$^+$物种的催化下与烯烃发生耦合反应, 最终生成芳烃产物. (3) 正丁烷在Zn-OH$^+$和(Zn-O-Zn)$^{2+}$物种的催化下, 发生脱氢和异构化反应产生烯烃. 部分烯烃可通过与CO耦合或烯烃发生聚合、环化、脱氢等过程生成芳烃产物.

综上所述, 本文深入探讨了CO_2与正丁烷在Zn-ZSM-5催化剂上的耦合反应机制. 通过系统研究, 建立了催化剂中Zn物种与催化性能之间的构-效关系, 并提出了耦合反应的具体路径. 本文不仅有助于深入理解Zn-ZSM-5的催化作用机制, 而且对于未来设计和开发更高效的催化体系具有重要的参考价值.

关键词: 耦合反应; CO_2利用; 锌的引入; Zn-OH$^+$; (Zn-O-Zn)$^{2+}$; ZSM-5

收稿日期: 2024-03-05. 接受日期: 2024-04-10. 上网时间: 2024-06-20.
*通讯联系人. 电子信箱: zhengxiyu@dicp.ac.cn (于政锡), liuzm@dicp.ac.cn (刘中民).
基金来源: 国家自然科学基金(21991093, 21991092, 21991090); 科技部国家重点研发计划(2022YFE0116000); 中国科学院战略性先导科技专项(XDA29000000).